

# Comparative Scatter and Dose Performance of Slot-Scan and Full-Field Digital Chest Radiography Systems<sup>1</sup>

Ehsan Samei, PhD  
Joseph Y. Lo, PhD  
Terry T. Yoshizumi, PhD  
Jonathan L. Jesneck, BS  
James T. Dobbins III, PhD  
Carey E. Floyd, Jr, PhD  
H. Page McAdams, MD  
Carl E. Ravin, MD

Published online before print  
10.1148/radiol.2353040516  
Radiology 2005; 235:940–949

#### Abbreviations:

CCD = charge-coupled device  
DQE = detective quantum efficiency  
SNR = signal-to-noise ratio  
TLD = thermoluminescent dosimeter

<sup>1</sup> From the Duke Advanced Imaging Laboratories, Department of Radiology (E.S., J.Y.L., T.T.Y., J.L.J., J.T.D., C.E.F., H.P.M., C.E.R.), Department of Biomedical Engineering (E.S., J.Y.L., J.L.J., J.T.D., C.E.F.), Department of Physics (E.S.), and Radiation Safety Division (T.T.Y.), Duke University Medical Center, DUMC 3302, Durham, NC 27710. Received March 18, 2004; revision requested May 25; revision received July 22; accepted August 19. **Address correspondence** to E.S. (e-mail: [samei@duke.edu](mailto:samei@duke.edu)).

Authors stated no financial relationship to disclose.

#### Author contributions:

Guarantors of integrity of entire study, E.S., J.T.D., C.E.R.; study concepts and design, E.S., J.Y.L., T.T.Y., J.T.D., C.E.F., H.P.M., C.E.R.; literature research, E.S., J.Y.L., T.T.Y., J.T.D., C.E.F.; experimental studies, all authors; data acquisition, E.S., J.Y.L., T.T.Y., J.L.J.; data analysis/interpretation, all authors; statistical analysis, E.S., J.Y.L., T.T.Y.; manuscript preparation, E.S., J.Y.L., T.T.Y., J.T.D., C.E.F.; manuscript definition of intellectual content, E.S., J.Y.L., T.T.Y.; manuscript editing, E.S., J.Y.L., T.T.Y., J.T.D., H.P.M., C.E.R.; manuscript revision/review and final version approval, all authors

© RSNA, 2005

**PURPOSE:** To evaluate the scatter, dose, and effective detective quantum efficiency (DQE) performance of a slot-scan digital chest radiography system compared with that of a full-field digital radiography system.

**MATERIALS AND METHODS:** Scatter fraction of a slot-scan system was measured for an anthropomorphic and a geometric phantom by using a posterior beam-stop technique at 117 and 140 kVp. Measurements were repeated with a full-field digital radiography system with and without a 13:1 antiscatter grid at 120 and 140 kVp. For both systems, the effective dose was measured on posteroanterior and lateral views for standard clinical techniques by using dosimeters embedded in a female phantom. The effective DQEs of the two systems were assessed by taking into account the scatter performance and the DQE of each system. The statistical significance of all the comparative differences was ascertained by means of *t* test analysis.

**RESULTS:** The slot-scan system and the full-field system with grid yielded scatter fractions of 0.13–0.14 and 0.42–0.48 in the lungs and 0.30–0.43 and 0.69–0.78 in the mediastinum, respectively. The sum of the effective doses for posteroanterior and lateral views for the slot-scan system ( $0.057 \text{ mSv} \pm 0.003$  [ $\pm$  standard deviation]) was 34% lower than that for the full-field system ( $0.086 \text{ mSv} \pm 0.001$ ,  $P < .05$ ) at their respective clinical peak voltages (140 and 120 kVp, respectively). The effective DQE of the slot-scan system was equivalent to that of the full-field system in the lung region but was 37% higher in the dense regions ( $P < .05$ ).

**CONCLUSION:** The slot-scan design leads to marked scatter reduction compared with the more conventional full-field geometries with a grid. The improved scatter performance of a slot-scan geometry can effectively compensate for low DQE and lead to improved image quality.

© RSNA, 2005

In the past decade, an increasing number of dedicated digital imaging devices have been developed for chest imaging. Many of these devices have been of the flat-panel type, which includes arrays of thin-film transistors coupled to either photoconductors (direct detection technology) (1) or to photodiodes with scintillators (indirect detection) (2). Other methods have included arrays of charge-coupled device (CCD) or complementary metal oxide semiconductor detectors (3,4) and a selenium-coated drum scanned with electrometers (5). Described in terms of the detective quantum efficiency (DQE), a common metric used to describe the exposure efficiency of a detector on the basis of its response to the primary x-ray radiation, most of these detectors have shown DQEs superior to those of screen-film or computed radiographic detectors (2,6–8). This improved DQE has enabled improved image quality per unit exposure (or consistent quality at reduced exposure) and has made possible various advanced applications that rely on high signal-to-noise ratio (SNR) and quantum efficiency.

While the concept of the DQE applies to the detector response to primary radiation, the unwanted detection of scattered photons at chest radiography has long been recognized as

a source of image quality degradation in terms of reduced image contrast and increased noise. Scattered x-rays can account for 95% of the detected x-ray flux in the mediastinum and up to 70% in the lung on radiographs acquired without a grid (9,10). By adding an unknown non-uniform background to the image, scatter degrades contrast and relative noise (expressed in terms of variance of the detector signal value divided by the mean detector signal value squared) on the image by a factor equal to the value of the scatter fraction. In other words, on a region of an uncompensated radiograph with a scatter fraction of 95%, only 5% of the original primary contrast remains. While this reduction in contrast can be remedied by means of postprocessing, the contribution of scattered radiation to image noise may not be readily correctable.

Over the years, various techniques have been developed to reduce the contribution of scattered photons to the image. The uses of antiscatter grids (11,12) and air gaps (13) have by far been the most common techniques. A grid can reduce the scatter fraction from 95% down to 65% in the mediastinum and from 70% down to 20% in the lung (11). However, while grids reject scattered photons, they also reduce the detection efficiency for primary photons, which leads to an increase in image noise for the same patient entrance exposure. The net result is an increase in SNR at the cost of an increase in patient dose. Air gaps similarly reduce detected scattered photons but can lead to increased patient dose and to magnification blur. To overcome these fundamental limitations, the use of scanning beam and slit devices has been proposed (12,14–16). These techniques offer scatter rejection without compromising the detection of primary photons. However, a previous commercial implementation of the scanning slot chest radiography system did not reject scatter better than a standard grid, possibly because of the large width of the slot (4 cm) for that system (17) or because of suboptimal tuning of the beam and detector slots.

A dedicated digital chest radiography system with a scanning slot apparatus has recently become commercially available. The system uses a small field array of detector elements that travel with a scanning slot, four times narrower than that of the previous implementation, to construct a full-field chest radiograph. A report of a recent study provided the resolution and DQE performance and the preliminary scatter performance of the new system (18). The purpose of our cur-

**TABLE 1**  
Basic Physical Specifications of the Evaluated Slot-Scan and Full-Field Systems

Characteristic	Slot-Scan System	Full-Field System
Capture element thickness (mm)*	0.5	Unspecified
Detector fill factor (%)	87	Unspecified
CCD pixel pitch (mm)	0.162 × 0.081	NA
Image pixel pitch (mm)	0.162 × 0.162	0.2 × 0.2
Image matrix size	2736 × 2736	2048 × 2048
Subdetector size (cm)	5.5 × 1.1	NA
Detector size (cm)	44.3 × 1.1	41.0 × 41.0
Image area (cm)	44.3 × 44.3	41.0 × 41.0
Scanning time (sec)	1.3	NA
Dwell time	32 msec†	mAs/mA × 1000
Source to image distance (cm)‡	173.7	183
Air gap (cm)	9.3	~3.9
Antiscatter grid		
Grid ratio	NA	13:1
Lines per centimeter	NA	78
Standard filtration (mm)	2.0 Al, 0.3 Cu	1.9 Al, 0.2 Cu
Half-value layer at 140 kVp (mm)	9.5 Al	8.7 Al

Note.—Al = aluminum, Cu = copper, NA = not applicable.

\* Thallium-doped cesium iodide scintillator for both systems.

† Calculated as scanning width (1.1 cm) × scanning time (1.3 sec)/scanning length (44.3 cm).

‡ Measured to the cover plate of the system.

rent study was to evaluate the scatter, dose, and effective DQE performance of the slot-scan digital chest radiography system compared with that of a more conventional full-field radiography system.

## MATERIALS AND METHODS

### Slot-Scan Imaging System

Physical specifications of the slot-scan imaging system are shown in Table 1 and Figure 1a. The slot-scan system (ThoraScan; Delft Imaging Systems/Nucletron, Veenendaal, the Netherlands) is composed of a moving CCD-based slot detector in conjunction with a dedicated x-ray tube and high-frequency generator capable of producing a moving fan beam of x-rays. The detector consists of eight 5.5 × 1.1-cm subdetectors tiled together to create a 44 × 1.1-cm sensitive area. Each subdetector is made of a thallium-doped cesium iodide scintillation layer fiberoptically coupled to a CCD.

The system uses the slot scanning geometry to acquire the chest radiograph with no antiscatter grid in place. The narrow fan beam synchronized with the movement of the detector assembly scans the patient, moving upward. Automatic exposure control is achieved by means of a low-dose partial downward initial scanning from which the appropriate level of tube current for subsequent scanning is determined. The image data are continuously read from the CCDs as the patient is scanned by means

of the time-integration method (19,20). After scanning, the image data are sent to an associated processing workstation, where the data are resampled into equal increments in the orthogonal directions and are corrected for nonuniformities through gain, offset, and bad-pixel calibration (21). The image data are finally postprocessed by using a multiscale image processing algorithm and are tone scaled for proper display (22).

Prior to image acquisition, the imaging system was calibrated according to the manufacturer's guidelines at 117 kVp and 2.4 mAs with 2.0 mm of added copper filtration. The copper filtration was removed for subsequent image acquisitions. The system performance was evaluated at 117 and 140 kVp, with 0.3 mm of added copper filtration. The latter is the setting suggested by the manufacturer for most patients, while the former is recommended for small patients.

### Full-Field Imaging System

Physical specifications of the full-field imaging system are shown in Table 1 and Figure 1b. The full-field imaging system (XQ/i; GE Medical Systems, Milwaukee, Wis) is composed of a thallium-doped cesium iodide scintillation layer directly coupled to a flat-panel amorphous silicon thin-film transistor array. The system is conventionally used with a 13:1 antiscatter grid (Mitaya Manufacturing, Tokyo, Japan) with 78 lines per centimeter,

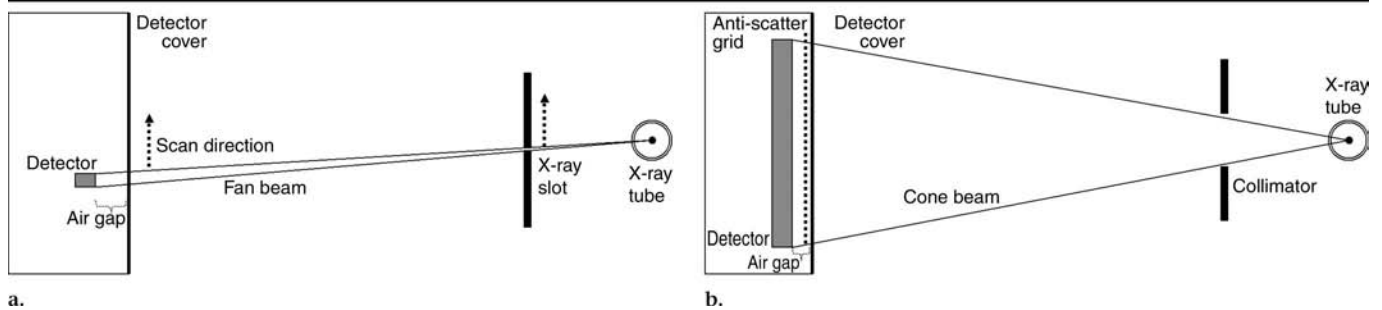


Figure 1. The general internal schematics of the (a) slot-scan and (b) full-field chest radiography systems.

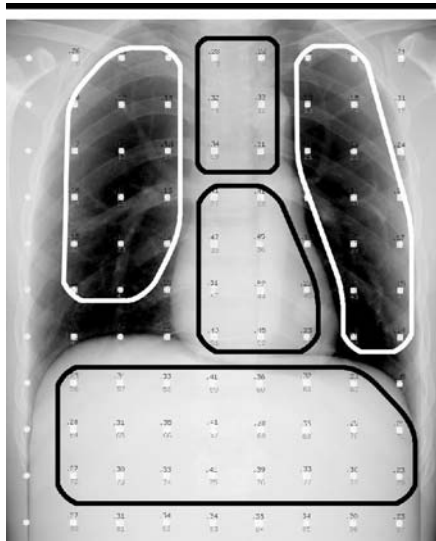


Figure 2. Radiograph of an anthropomorphic phantom with associated beam stops used for scatter fraction measurements. Highlighted areas indicate the locations used for the assessment of scatter fraction in the lungs, mediastinum, and retrocardiac and subdiaphragmatic regions. Similar region designations were used on the geometric phantom images.

180-cm focal distance, 20- $\mu$ m lead strips, and aluminum interspace.

Prior to image acquisition, the imaging system was calibrated according to the manufacturer's guidelines with 20 mm of added aluminum filtration. The aluminum filtration was removed for subsequent image acquisitions. The system performance was evaluated at 120 kVp with 0.2 mm of added copper filtration, which is the beam quality suggested by the manufacturer for normal use. In addition, measurements were obtained at 140 kVp to compare the results with those obtained at 140 kVp for the slot-scan system.

### Scatter Measurements

The scattered radiation performance of the two imaging systems was evaluated

in terms of scatter fraction by using an anthropomorphic (Humanoid Systems, Carson, Calif) and a geometric chest phantom (23). The anthropomorphic phantom, designed to correspond to a human of average build (175 cm in height, 73.5 kg in mass), was augmented with two additional 2.5-cm-thick slabs of acrylic (one posterior and one anterior). In previous experiments, this augmentation was found to provide scatter fractions that are closer in value to those measured in clinical practice (24). The geometric phantom consisted of interleaved slices of acrylic designed to approximate the attenuation and scatter characteristics of the chest, specifically 11.2 cm of acrylic in the lung, 20.0 cm in the mediastinum, and 22.3 cm in the subdiaphragm. Note that the geometric phantom did not include a retrocardiac region.

Each phantom was placed in a posteroanterior orientation. An array of beam stops (14  $\times$  16 array, 25-mm spacing, each beam stop a cylinder of 3-mm diameter and 6-mm height embedded in a 6-mm sheet of acrylic) was placed posterior to each phantom (ie, on the tube side of the phantom), and images were acquired with postprocessing and tone scaling turned off and with automatic exposure control set to manual techniques. For the slot-scan system, the images were acquired at 117 and 140 kVp with exposure set at four times the predetermined photo-timed milliamperes-second settings to ensure quantitative accuracy in measuring the low exposures behind the beam stops. For the full-field system, scatter measurements were made at 120 and 140 kVp at two times the photo-timed milliamperes-seconds with and without the standard antiscatter grid in place.

For each beam stop, the scatter fraction was then measured as the ratio of the exposure behind the beam stop to that in an area immediately surrounding the beam stop by using a technique previ-

ously developed at our laboratory (9,25). Only beam stops in specific anatomic regions were used for analyses; all others were disregarded. The scatter fractions in each anatomic region were then computed from averages obtained from the beam stops located in that region. The number of beam stops in each anatomic region varied between the two systems because of differences in detector size, magnification, and beam stop array placement. Nonetheless, the number of beam stops was always adequate to characterize the scatter fraction in each region. For the slot-scan system, the number of beam stops projected in the lung, mediastinum, retrocardiac region, and subdiaphragmatic region of the images were 62, 32, 0, and 22 in the geometric phantom and 30, 6, 10, and 23 in the anthropomorphic phantom, respectively (Fig 2). The corresponding numbers for the full-field system were 52, 34, 0, and 11 in the geometric phantom and 32, 7, 11, and 18 in the anthropomorphic phantom, respectively. The scatter measurements were obtained primarily by two of the authors (J.Y.L., J.L.J.), with additional assistance from the other authors.

### Dose Measurements

The dose performance of each system was evaluated by using an adult female anthropomorphic phantom (CIRS, Norfolk, Va) embedded with thermoluminescent dosimeters (TLDs) (Fig 3). The phantom was different from those used for the scatter measurements because those phantoms were not designed for embedding dosimeters. The TLDs (Harshaw TLD-100; Thermo Electron, Santa Fe, NM) were embedded in 20 locations within the phantom. The locations included the left and right sides of the phantom. Four locations within each breast were also included and corresponded to 12-, 3-, 6-, and 9-o'clock positions while facing the breast. Two TLD chips were placed

within each organ location, and the mean value of two readings was used for the assessment of dose at that location. The dose error bars associated with each TLD-estimated dose level were estimated from the data obtained in a separate experiment, in which relative error was assessed as a function of dose level by irradiating a series of five TLD chips (26). Prior to data acquisition, the TLDs were calibrated by measuring their response to a simulated x-ray beam with a comparable peak voltage and half-value layer. The details of the TLD calibration method can be found elsewhere (26). The dosimetry took into account the active marrow distribution in various bones within the body (27).

The phantom was placed in either a posteroanterior or a left-lateral orientation. For lateral views, the beam entered the phantom from the right side. The measurements on the slot-scan system were made at 117 and 140 kVp. Those on the full-field system were made at 120 and 140 kVp. For each system and technique, multiple images were acquired at milliamperes-second settings higher than clinical settings to produce high signals in the TLDs.

After exposure, the TLD chips were extracted and read by using a TLD reader (Auto TLD Reader Model QS 5500; Harshaw, Solon, Ohio). Organ dose values were normalized by the total applied milliamperes-second values and then were multiplied by the standard clinical photo-timed milliamperes-second values for the phantom. In this manner, the measured dose values were scaled to be representative of clinical doses. For organs for which the dose was measured at multiple locations (eg, breast), the maximum measured dose value was used as the most conservative estimate of radiation risk and organ dose. The effective dose was then calculated by using the weighting factors published in *International Commission on Radiological Protection Publication 60* (28). The overall error for the effective dose was estimated by using the quadrature summing of the errors for each organ within the phantom. The dose measurements were obtained primarily by one of the authors (T.T.Y.), with additional assistance from the other authors.

### Effective DQE Calculations

While the DQE is used to describe the performance of a digital radiographic detector without scatter, in the presence of scattered radiation and additional atten-

uating layers, an effective DQE,  $DQE_{\text{eff}}$  of a radiographic system may be defined as  $DQE_{\text{eff}} = t(1 - SF)DQE$ , where  $t$  is the transmission of the primary x-rays by the elements of the imaging chain before the detector,  $SF$  is the scatter fraction, and  $DQE$  is the conventionally measured DQE in the absence of the antiscatter grid and scattered radiation (18). This definition is consistent with an earlier extension of the DQE concept by Wagner et al (29) to characterize the performance of antiscatter grids.

By assuming equivalent x-ray attenuation through the detector cover plates of the two systems, the effective DQEs of the systems were assessed from the measured scatter fractions with the anthropomorphic phantom, a grid transmission measurement, and prior reports of the DQE performance of the two systems. By neglecting the frequency-dependent components of the scattered radiation, the measured DQE values at 0.15 cycles per millimeter were used as surrogates for the DQE at zero frequency. Those values were previously reported to be 0.45, 0.18, and 0.16 for the full-field system at 120 kVp, the slot-scan system at 117 kVp, and the slot-scan system at 140 kVp, respectively (6,18). For the full-field system, it was assumed that the DQE at 140 kVp was lower than that at 120 kVp by the same fraction as that measured for the slot-scan system, that is, full-field DQE (0.15 cycles per millimeter, 140 kVp) is  $0.45 \cdot 0.16/0.18 = 0.4$ .

For the full-field system, the primary transmission through the grid was measured at the standard clinical beam quality (120 kVp, 0.2 mm of added copper filtration). This measurement was obtained by placing a calibrated ionization chamber (model 10×5-6 ionization chamber and model 1015 x-ray monitor; Radcal, Monrovia, Calif) on the central axis of the beam at a distance of 100 cm from the focal spot. The beam was collimated to only envelope the ionization chamber, with 3-cm margins on each side. The ratio of measured exposures at a fixed high milliamperes-second with and without the grid at the collimator was used to calculate the grid primary transmission. The measurement indicated a grid primary transmission of 0.65. Because the chamber was placed on the central axis and away from the detector, the measurements were not affected by off-focus placement of the grid or back-scattered radiation. All the effective DQE calculations and required measurements were made by one author (E.S.) and the results were examined by all.

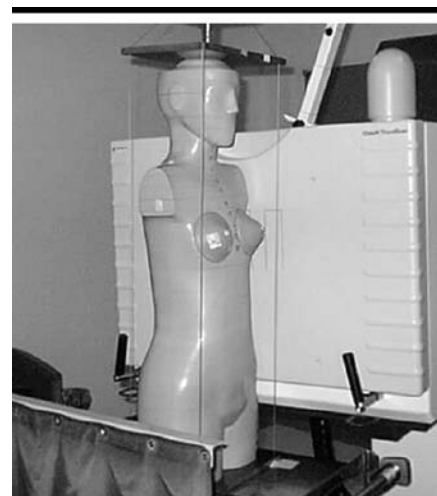
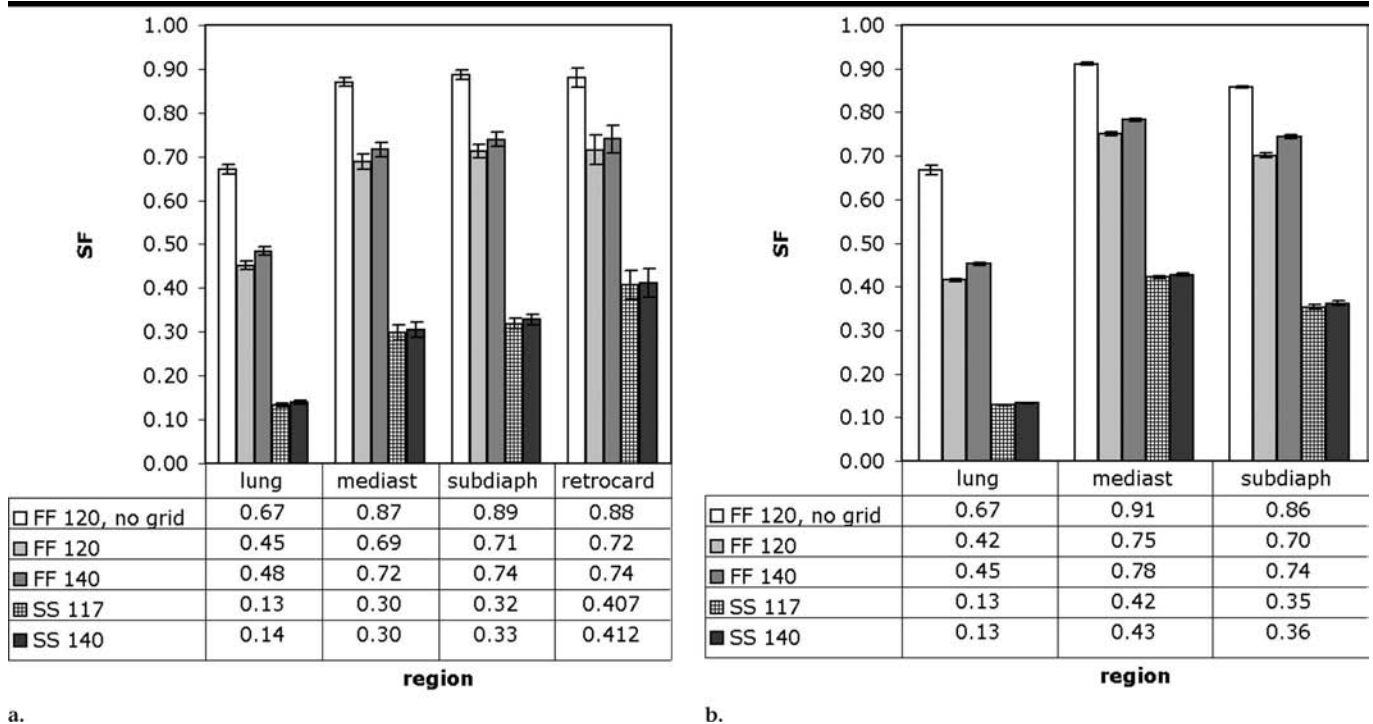


Figure 3. The setup for measurement of effective dose.

To further verify the relative effective DQE of the two systems, we acquired images of the anthropomorphic chest phantom with the two systems and their corresponding clinical techniques (slot scan, 140 kVp; full field, 120 kVp with grid) with photo-timed exposures. The images were acquired by one author (E.S.) and were subjectively evaluated by all authors, independently and by consensus, to identify any substantial errors in the conclusions drawn from the dose and the effective DQE results.

### Statistical Analysis

For the scatter fraction measurements, the differences between the two imaging systems and those between the full-field system with and without the grid were examined by using a two-tailed  $t$  test, assuming unequal variances. For cases in which the two experimental conditions included an equal number of beam stops (ie, the full-field system with and without the grid and each system at different beam qualities), a paired  $t$  test was performed; otherwise, an unpaired  $t$  test was performed. Similar analysis was undertaken for statistical significance of differences observed in the calculated effective DQE figures, with the assumption that scatter fraction was the only source of uncertainty. For dose measurements, the differences between the two systems were similarly examined by using a  $t$  test. Statistically significant differences were defined at  $P$  values less than .05. The statistical analyses were performed by using a spreadsheet program (Excel 2000; Microsoft, Redmond, Wash). The calculations were performed primarily by three



**Figure 4.** Graphs of scatter fraction (*SF*) measurements for the slot-scan (*SS*) and full-field (*FF*) systems at comparable beam qualities by using (a) an anthropomorphic and (b) a geometric chest phantom. Error bars indicate  $\pm 1$  standard error. The data indicate that the addition of a grid reduces scatter fraction for the full-field system, but the reduction does not reach the levels afforded with the slot-scan system. *mediast* = Mediastinum, *retrocard* = retrocardiac region, *subdiaph* = subdiaphragmatic region.

of the authors (J.Y.L., T.T.Y., E.S.), with additional input from our statistical consultant.

## RESULTS

### Scatter Results

The measured scatter fractions for both imaging systems at two energy levels are presented in graphic and tabular form in Figure 4a and 4b for measurements with the anthropomorphic and geometric phantoms, respectively. The most dramatic difference in the measured scatter fractions is observed when comparing the values from the two systems. For the full-field system, the values are consistent with those expected with the use of a high-efficiency grid. In the region of the phantoms that represented the lung, scatter fractions of 40%–45% were measured, while in the mediastinum the values were larger, as expected: 70%–80%, with slight differences between the mediastinal, retrocardiac, and subdiaphragmatic regions. The slot-scan system showed dramatically reduced scatter fractions for all regions in both phantoms. For the lung region, the scatter fractions were about 13%. For the mediastinum, they were in the 30%–40% range, while

in the subdiaphragmatic region, they ranged from 32% to 36%. When compared with measurements for the full-field system, these slot-scan measurements represent a marked decrease in scatter fraction by a factor of about three in the lung, a factor of two in the mediastinum, and a factor between two and three in the subdiaphragmatic region. For the retrocardiac region of the anthropomorphic phantom, this is a decrease by a factor just less than two.

Scatter fractions measured for the full-field system with the antiscatter grid removed were 67% for the lung and 86%–91% for the denser (mediastinal, subdiaphragmatic, and retrocardiac) regions. With both phantom results at 120 kVp, the grid reduced scatter fractions by approximately 22%–25% in the lung and 16%–18% in the denser regions; the corresponding values for the slot-scan system were 54% and 47%–57%, respectively, which suggests a substantial advantage of the slot-scan technique over the grid for scatter reduction. For each system, there is no appreciable difference between the measured scatter fractions for the two energy levels examined with either of the two phantoms.

In comparing the measured scatter fractions, the differences between the two systems, between the grid and no grid conditions, and between different beam qualities were all statistically significant by a large margin ( $P < .001$ ).

### Dose Results

Tables 2 and 3 summarize the dose performance of the two systems. Notable for the left-lateral exposure is the variation in organ doses because of geometric distance and attenuation. For example, for the slot-scan system, the lateral lung dose ratio was 4.2 (109.0  $\mu$ Gy in right lung  $\div$  25.9  $\mu$ Gy in left lung) at 117 kVp and 3.7 at 140 kVp. For the full-field digital system, the lateral lung dose ratio was 3.7 at 120 kVp and 4.3 at 140 kVp. Similarly, the lateral 9-o'clock breast dose ratio was 5.4 at 117 kVp and 5.1 at 140 kVp for the slot-scan system and 5.8 at 120 kVp and 4.8 at 140 kVp for the full-field digital system. Overall, the effective dose for the lateral view with the slot-scan system was a factor of 1.3 higher than that for the posteroanterior view at 117 kVp and was a factor of 1.6 higher at 140 kVp. This factor was notably higher (ie, a factor of

3.6 at both 120 kVp and 140 kVp) for the full-field digital system tested (Table 3).

In the comparison of the two systems at their corresponding clinical peak voltage settings (120 kVp for full field and 140 kVp for slot scan), the slot-scan system delivered a 16% ( $1 - 0.022/0.019$ ) higher effective dose for the posteroanterior exposure, but this difference was not statistically significant ( $P > .05$ ). However, for the lateral exposure, the slot-scan system delivered a significantly ( $P < .05$ ) lower effective dose, which led to an approximately 34% ( $1 - 0.057/0.087$ ) lower total dose (posteroanterior and lateral) compared with the total dose delivered by the full-field system ( $P < .05$ ).

### Effective DQE Results

Figure 5 presents values for the effective DQE. For the full-field system, the presence of the grid was generally advantageous, particularly in the dense regions. In the lung region, the two systems at their corresponding operating conditions (slot scan, 140 kVp; full field, 120 kVp with grid) performed equally well. However, in the denser regions, the slot-scan system yielded superior performance compared with the full-field system by an average of 37%, which indicates that a more efficient scatter rejection of a system can effectively compensate for its lower DQE. The comparable dose figures of the two systems as noted here serve as a secondary confirmation of this observation. All the differences in the effective DQE measurements were statistically significant ( $P < .05$ ).

Figure 6 shows the images from our subjective evaluation. Given the differences in the image processing techniques applied by the two systems, the images cannot be objectively compared. However, from a subjective standpoint, the images obtained with the slot-scan system show relatively more detail and less noise. The difference in the lung regions is less pronounced, as predicted from the comparable effective DQEs of the two systems in that region, and, in fact, the slightly improved details obtained with the slot-scan system may be attributed to the statistically insignificant 16% greater radiation dose for that system (0.022 and 0.019 mSv,  $P > .05$ ; Tables 2, 3). However, in the mediastinal region, the difference between the effective DQE of the two systems was more pronounced, and, thus, the difference in the noise level of the corresponding images is more readily discernable. These subjective observa-

**TABLE 2**  
Organ Dose and Effective Dose Measurements with the Slot-Scan System for Photo-timed Posteroanterior and Left-Lateral Orientations

Organ	117 kVp		140 kVp	
	Posteroanterior at 3.0 mAs*	Left Lateral at 4.0 mAs*	Posteroanterior at 2.0 mAs*	Left Lateral at 3.2 mAs*
Lung				
Right	NA	109.0 ± 13.0	NA	117.0 ± 14.0
Left	111.0 ± 18.0	25.9 ± 5.0	88.9 ± 14.6	31.9 ± 6.0
Breast				
Right				
12 o'clock	NA	136.0 ± 20.0	NA	207.0 ± 24.0
3 o'clock	41.2 ± 8.2	87.3 ± 14.9	35.1 ± 7.0	133.0 ± 19.0
6 o'clock	NA	133.0 ± 20.0	NA	198.0 ± 24.0
9 o'clock	NA	170.0 ± 22.0	NA	245.0 ± 25.0
Left				
12 o'clock	NA	20.9 ± 4.5	NA	31.5 ± 6.5
3 o'clock	28.8 ± 6.0	17.0 ± 3.7	18.0 ± 1.6	24.6 ± 5.2
6 o'clock	NA	19.8 ± 4.2	NA	32.0 ± 6.5
9 o'clock	NA	31.7 ± 6.5	NA	48.2 ± 9.3
Bone marrow	31.9 ± 3.4	37.0 ± 3.1	24.5 ± 3.0	47.2 ± 5.9
Effective dose (mSv)	0.028 ± 0.003	0.038 ± 0.002	0.022 ± 0.002	0.035 ± 0.002

Note.—Data are ± 1 standard deviation, and except where noted, data are measured in micrograys. NA = not applicable.

\* Effective tube current, calculated as follows: (indicated nominal tube current)/(beam-on time, 1.5 sec) × (slot width, 1.1 cm) × (scanning time, 1.3 sec)/(scanning length, 44.3 cm). Calculations were made with the assumption of a rectangular x-ray beam profile.

**TABLE 3**  
Organ Dose and Effective Dose Measurements with the Full-Field System for Photo-timed Posteroanterior and Left-Lateral Orientations

Organ	120 kVp		140 kVp	
	Posteroanterior at 2.07 mAs	Left Lateral at 6.74 mAs	Posteroanterior at 1.37 mAs	Left Lateral at 5.10 mAs
Lung				
Right	NA	118.0 ± 13.0	NA	178.0 ± 4.0
Left	68.8 ± 1.7	32.0 ± 5.9	55.4 ± 1.4	41.5 ± 1.0
Breast				
Right				
12 o'clock	NA	178.0 ± 14.0	NA	197.0 ± 5.0
3 o'clock	23.2 ± 0.6	111.0 ± 13.0	15.8 ± 0.4	120.0 ± 3.0
6 o'clock	NA	193.0 ± 14.0	NA	182.0 ± 5.0
9 o'clock	NA	231.0 ± 14.0	NA	241.0 ± 5.0
Left				
12 o'clock	NA	29.3 ± 5.5	NA	26.7 ± 1.7
3 o'clock	23.7 ± 0.6	22.7 ± 4.5	24.7 ± 0.6	36.7 ± 1.7
6 o'clock	NA	33.2 ± 6.1	NA	28.2 ± 1.7
9 o'clock	NA	44.0 ± 7.5	NA	50.0 ± 1.7
Bone marrow	18.6 ± 0.3	40.5 ± 3.2	17.2 ± 0.3	60.0 ± 1.0
Effective dose (mSv)	0.019 ± 0.000	0.068 ± 0.001	0.017 ± 0.000	0.062 ± 0.001

Note.—Data are ± 1 standard deviation and, except where noted, are measured in micrograys. NA = not applicable.

tions confirm the predictions of the effective DQE observations.

### DISCUSSION

In the past 20 years, various technologies have been deployed to acquire digital chest radiographs. Among those, computed radiography, CCDs and complementary metal oxide semiconductor de-

vices, and flat-panel digital detectors have become commercially viable and are gradually replacing more conventional analog screen-film systems. One of the major goals in the development of these detector technologies has been the improvement of the DQE, which enables the acquisition of higher quality images with greater SNR at a lower dose. While other factors such as scatter and ana-

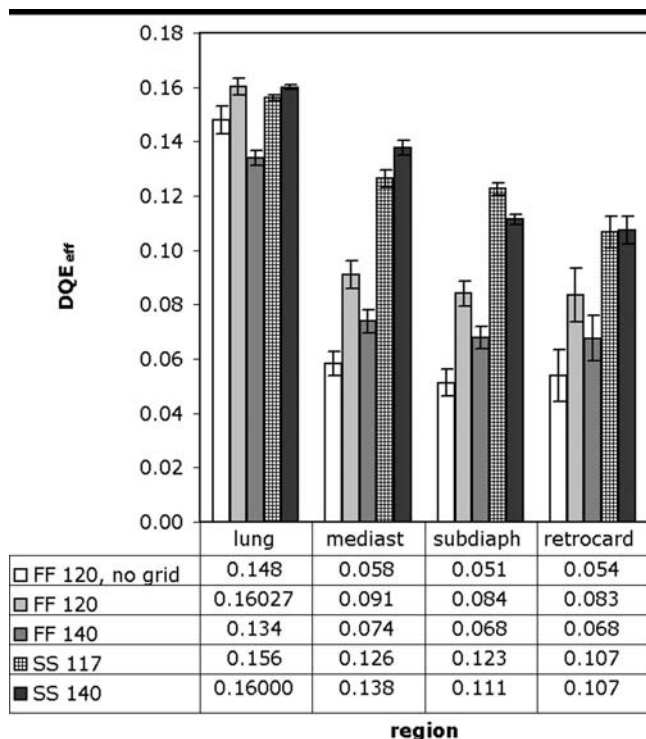


**Figure 5.** Graph of effective DQE ( $DQE_{eff}$ ) of the slot-scan (SS) and full-field (FF) systems after taking into consideration the scattered radiation (from anthropomorphic phantom measurements) and primary grid transmission (65%). Error bars indicate  $\pm 1$  standard error. Results indicate that in the lung the full-field and slot-scan systems perform similarly, but in the denser regions (mediastinal, retrocardiac, subdiaphragmatic regions), the slot-scan system offers higher SNR (at equivalent exposure) provided by its reduced scatter fraction.

tomic noise also affect image quality, in the absence of other objective measures, recent years have witnessed the emergence of the DQE as the primary index of image quality. Different technologies have different capabilities in that regard; flat-panel detectors have DQEs two to three times higher than those of computed radiography (6,21). CCDs and complementary metal oxide semiconductor devices have offered another solid-state alternative to flat-panel detectors for acquiring digital radiographs. However, because of the low efficiency of their required optical coupling, these detectors generally offer a lower DQE compared with that of flat-panel detectors (18,30,31).

While the DQE describes an important aspect of the performance of an imaging system, because it characterizes the inherent image quality characteristics of the detector employed by a system, it does so in the absence of scattered radiation. As described previously, scatter can account for up to 70% of the detected x-rays in the lung and 95% in the mediastinum on a chest radiograph. Most dig-

ital detector systems employ the traditional antiscatter grid or air gap for scatter rejection. However, there is still considerable scattered radiation even with the use of such devices; it accounts for up to 35% of the detected x-rays in the lung and 65% in the mediastinum. This residual scattered radiation reduces image contrast and increases noise. While digital images can be digitally postprocessed to improve contrast, most postprocessing approaches (such as window and level adjustments) also increase the perceivable noise on the image, so that the resulting contrast-to-noise ratio remains limited. Nonlinear postprocessing techniques to remove scatter while maintaining or improving contrast-to-noise ratio have been previously reported but have not been implemented commercially.

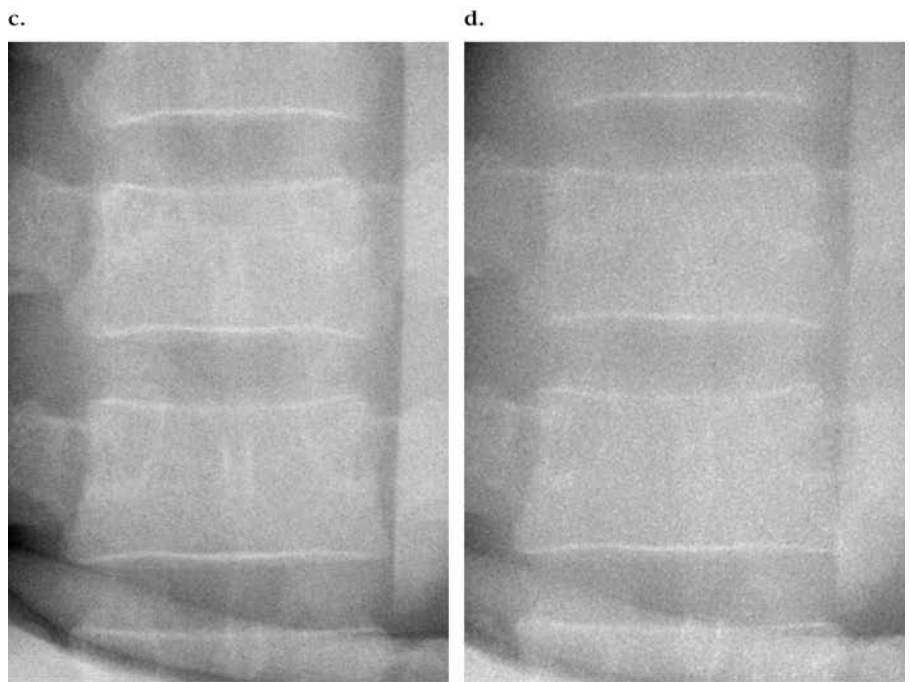
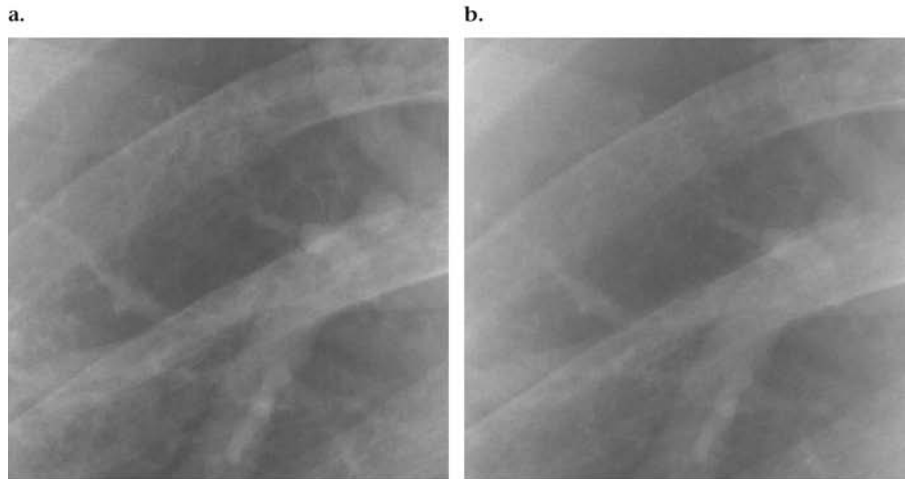
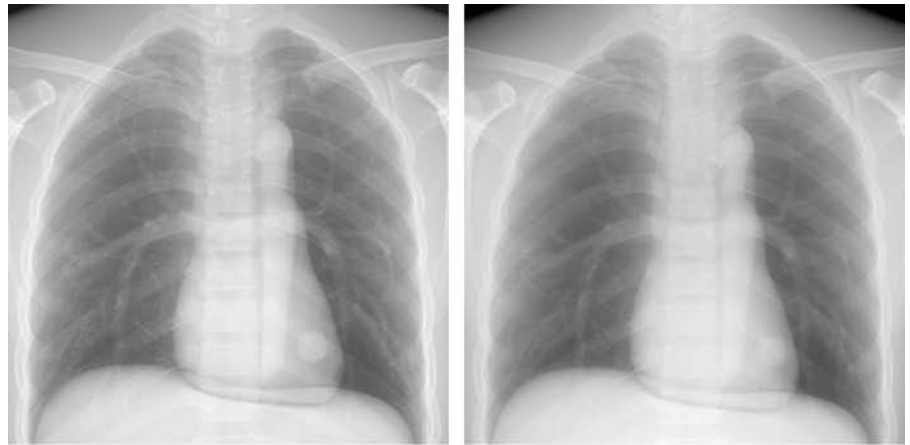
A different approach for scatter reduction is the use of scanning radiography with one or more slits or slots (14). While other digital slot-scan mechanisms have been explored in the past, the CCD-based imaging system evaluated in this study was the first commercial digital version of the slot scanning technology for ded-

icated chest radiography. The system offers a notably narrow slot width (1 cm) with an additional 9.3-cm air gap. Our scatter fraction measurements indicate that the slot-scanning method used with this system offers a notable reduction in scattered radiation, which leads to improved image SNR at a comparable patient dose. Compared with measurements obtained by using a full-field digital chest radiography system with a typical 13:1 antiscatter grid, the slot-scan system yielded scatter fractions that were less than one-half of those in the mediastinal and subdiaphragmatic regions and less than one-third of those in the lung regions.

The scatter fractions measured for this slot-scan system compare favorably with those of previous systems with a similar geometry. According to previous measurements obtained by our group, a commercial analog slot-scan system known as advanced multiple-beam equalization radiography, or AMBER, did not reduce scatter fractions in comparison with a full-field system when used without exposure equalization. Sorenson et al (14) reported on a noncommercial system with a 1-cm scanning slot, 18-cm air gap, and 12:1 grid. Compared with the results of the current study, the scatter fractions from that previous study were higher in the lung (0.21) and comparable or lower in denser regions (0.30–0.39). Recalling that the current system uses an approximately 1-cm scanning slot, a smaller 9.3-cm air gap, and no grid, the system likely has superior design elements and better tuning of the beam and detector slots, thereby providing effective scatter rejection comparable to or better than those in previous reports (ie, 0.13 scatter fraction in the lung and 0.35–0.43 in denser regions).

While our findings indicate a notable difference between the scatter rejections of the tested slot-scan and full-field imaging systems, that difference should be attributed to the image acquisition geometry used with the two systems and not to the specific performance of the detectors employed reflected in their relative DQE. The slot-scan system offers a DQE 2.5 times lower than that of the full-field system (6,18). However, our measurements indicate that the system imparts two to three times less scatter and a 34% lower overall examination dose. These observations suggest that relying on the DQE alone as a single index of image quality per unit exposure can lead to misleading conclusions when comparing the inherent performance of

**Figure 6.** Posteroanterior radiographs of the anthropomorphic phantom at clinical techniques by using the (a) slot-scan (140 kVp, 1.58 photo-timed effective mAs) and (b) full-field (120 kVp, 2.67 photo-timed mAs) systems. Images were processed according to the native respective processing of the two systems. Magnified and contrast-matched (by manipulating window width and level) areas of the lungs and the mediastinum with the (c, e) slot-scan and (d, f) full-field systems. The data indicate that at a somewhat equivalent exposure, images from the two systems show similar-quality details in the lung regions. However, in the denser regions, the slot-scan system offers lower noise, subjectively confirming the effective DQE findings.



various digital radiography systems. The limitation of the DQE stems from two aspects of the metric as follows: (a) The DQE is often used to characterize the performance of the detector alone, without the inclusion or consideration of other elements of the imaging system such as the antiscatter grid or air gap, and (b) the DQE only involves the detector response in terms of the detection of primary x-ray radiation. No scattering medium is present in the beam when the DQE measurements are obtained. As a consequence, although the DQE is an effective metric to characterize the intrinsic performance of an imaging detector, it does not reflect an important and ever present component of radiologic imaging and therefore falls short of characterizing the performance of an imaging system. Reliance on the DQE alone can lead to biases in rank ordering of different radiography systems (30,32).

The effective DQE metric defined in this article includes the effect of scattered radiation and transmission through supradetector elements, such as grids, on image quality. Our results show that while the native DQE of the slot-scan system is lower than that of the full-field system, the reduced scatter detection of the slot-scan system can compensate for its lower DQE, which leads to equivalent (in the lungs) and even improved (in the mediastinal and subcardiac-subdiaphragmatic areas) image quality in terms of SNR per unit exposure. Our dose measurements are, in general, consistent with this conclusion. However, it should be noted that the measured dose figures may not be directly compared with the effective DQE figures because the dose values were obtained with the systems in the photo-timed mode, while effective DQE values were exposure-normalized, reflecting the achievable SNR per unit ex-

posure. If a pseudo-linear relationship is assumed between effective dose and exposure in the 100–150 kVp range, the reported effective DQE figures can be used to calibrate the photo-timers to achieve consistent SNR values for clinical images across different imaging systems.

To our knowledge, this article is the first to present digital chest dosimetry results in terms of individual organ doses; this departs from a traditional skin entrance exposure description. Furthermore, we estimated the effective dose figures by using the *International Commission on Radiological Protection Publication 60* (28) weighting factors. Although individual organ doses are on the order of tens of micrograys, the TLD data showed clear differentiation of organ dose between the slot-scan and full-field digital systems. It is of interest to observe the dose reduction between right and left lungs and between right and left breasts in lateral views. The sum of posteroanterior and lateral effective dose figures was 0.057 mSv and 0.087 mSv for the slot-scan and full-field digital systems at their clinical settings of 140 and 120 kVp, respectively. The difference was statistically significant ( $P < .05$ ). In terms of risk, these values may pose negligible risks, but they serve as a useful dose index in comparing two digital chest systems.

The dose and scatter results reported from our study and the associated effective DQE are only relevant to a population of average-sized patients. However, in the patient population imaged in the United States, there are increasing numbers of patients with larger body mass. Because the scatter fraction increases with patient size, the removal of scattered radiation for larger patients would be even more important. While we have not obtained scatter measurements for larger body types, the dense regions of the chest phantoms examined demonstrated relatively larger scatter fractions. The data showed that the relative advantage of the slot-scan system is more pronounced for larger scatter fraction regions. Thus, it is reasonable to predict that the slot-scan system would be even more effective for larger patients.

Notwithstanding these implications in terms of scatter removal, full-field digital radiography systems offer some potential advantages in terms of image acquisition and aptitude for advanced x-ray–based imaging applications. The full-field digital radiography systems would require a lower level of tube loading than would an equivalent slot-scan system, since the

x-ray flux in the latter system would need to be maintained during a longer period of image acquisition (1.3 seconds in the case of the system tested in this study vs a few hundred milliseconds for a full-field system). Contrary to common notion, however, the longer acquisition time does not translate into potential for more patient motion artifacts. The reason is that at any incremental period of time during the slot-scan image acquisition (ie, a dwell time of 32 msec; Table 1), only a small fraction of the image (ie, an approximately 1-cm-wide horizontal band) is acquired. If the patient moves during that time interval, only a 1-cm-tall portion of the image will be blurred, whereas with the full-field system, the entire image will be affected. In addition, the current implementations of dual-energy and digital tomosynthesis imaging modalities require a large-area detector for rapid acquisition of multiple sequential images. The future developments in advanced applications with slot-scan detector systems may alter these conclusions regarding the relative merits of the two imaging methods.

The present study had limitations that should be taken into consideration. First, the effective DQE calculations did not take into account the spatial frequency component of scattered radiation and the effect of the grid on the frequency content of the image. The concept of effective DQE ideally should be extended beyond zero frequency through direct measurements. Second, because of design considerations, we were unable to use the same phantom for the scatter and dose measurements. While the figures are generally comparable, they might not be quantitatively related. These limitations will provide opportunities for future research in this area.

In summary, compared with conventional chest imaging systems with anti-scatter grids, the digital slot-scan imaging system offers a marked advantage in terms of scatter reduction and an associated improvement in the effective DQE, which leads to improved image quality. This advantage is more pronounced in areas of the image with high scatter fraction, such as the mediastinum and the subdiaphragmatic region. Because scatter fraction usually increases as patient body mass increases, it is expected that this advantage will be more pronounced for larger patients. Our subjective comparison of the quality of clinical chest images acquired with the two systems confirms this conclusion.

**Acknowledgments:** The authors acknowledge David M. Delong, PhD, of Duke University for reviewing the statistical analyses of this study. The authors further thank Greta Toncheva, MS, Giao Nguyen, MS, Lottie Barnes, BS, and Maksudur Sarder, MS, of Duke University for TLD dosimetry support, and Robert Saunders, MA, Nicole Ranger, MS, and Tom Boehringer, AAS, of Duke University for additional technical assistance.

## References

- Rowlands JA, Zhao W, Blevins IM, Waechter DF, Huang Z. Flat-panel digital radiology with amorphous selenium and active-matrix readout. *RadioGraphics* 1997; 17:753–760.
- Floyd CE Jr, Warp RJ, Dobbins JT 3rd, et al. Imaging characteristics of an amorphous silicon flat-panel detector for digital chest radiography. *Radiology* 2001; 218:683–688.
- Hejazi S, Trauernicht DP. System considerations in CCD-based x-ray imaging for digital chest radiography and digital mammography. *Med Phys* 1997; 24:287–297.
- Des Jardin W, Parks C, Doan H, Kurfiss N, Wetzel K. A large format high-performance CCD sensor for medical x-ray applications. In: Dobbins JT 3rd, Boone JM, eds. *Proceedings of SPIE: medical imaging 2000—physics of medical imaging*. Vol. 3977. Bellingham, Wash: International Society for Optical Engineering, 2000; 167–175.
- Neitzel U, Maack I, Gunther-Kohfahl S. Image quality of a digital chest radiography system based on a selenium detector. *Med Phys* 1994; 21:509–516.
- Samei E, Flynn MJ. An experimental comparison of detector performance for direct and indirect digital radiography systems. *Med Phys* 2003; 30:608–622.
- Samei E, Flynn MJ. An experimental comparison of detector performance for computed radiography systems. *Med Phys* 2002; 29:447–459.
- Dobbins JT 3rd, Ergun DL, Rutz L, Hinshaw DA, Blume H, Clark DC. DQE(f) of four generations of computed radiography acquisition devices. *Med Phys* 1995; 22:1581–1593.
- Floyd CE Jr, Baker JA, Lo JY, Ravin CE. Measurement of scatter fractions in clinical bedside radiography. *Radiology* 1992; 183:857–861.
- Niklason LT, Sorenson JA, Nelson JA. Scattered radiation in chest radiography. *Med Phys* 1981; 8:677–681.
- Sorenson JA, Niklason LT, Knutti DF. Performance characteristics of improved antiscatter grids. *Med Phys* 1980; 7:525–528.
- Barnes GT, Moreland RF, Yester MV, Witten DM. The scanning grid: a novel and effective bucky movement. *Radiology* 1980; 135:765–767.
- Sorenson JA, Floch J. Scatter rejection by air gaps: an empirical model. *Med Phys* 1985; 12:308–316.
- Sorenson JA, Nelson JA, Niklason LT, Jacobsen SC. Rotating disk device for slit radiography of the chest. *Radiology* 1980; 134:227–231.
- Plenkovich D, Sorenson JA, Kruger RA. Scatter rejection by electronic collimation. *Med Phys* 1986; 13:158–163.

16. Barnes GT, Brezovich IA, Witten DM. Scanning multiple slit assembly: a practical and efficient device to reduce scatter. *AJR Am J Roentgenol* 1977; 129:497-501.
17. Chotas HG, Floyd CE Jr, Dobbins JT 3rd, Lo JY, Ravin CE. Scatter fractions in AMBER imaging. *Radiology* 1990; 177:879-880.
18. Samei E, Saunders RS, Lo JY, et al. Fundamental imaging characteristics of a slot-scan digital chest radiographic system. *Med Phys* 2004; 31:2687-2698.
19. Holdsworth DW, Gerson RK, Fenster A. A time-delay integration charge-coupled device camera for slot-scanned digital radiography. *Med Phys* 1990; 17: 876-886.
20. Mainprize JG, Ford NL, Yin S, Tumer T, Yaffe MJ. A slot-scanned photodiode-array/CCD hybrid detector for digital mammography. *Med Phys* 2002; 29:214-225.
21. Samei E. Image quality in two phosphor-based flat panel digital radiographic detectors. *Med Phys* 2003; 30:1747-1757.
22. Prokop M, Neitzel U, Schaefer-Prokop C. Principles of image processing in digital chest radiography. *J Thorac Imaging* 2003; 18:148-164.
23. Chotas HG, Van Metter RL, Johnson GA, Ravin CE. Small object contrast in AMBER and conventional chest radiography. *Radiology* 1991; 180:853-859.
24. Baydush AH, Ghem WC, Floyd CE Jr. Anthropomorphic versus geometric chest phantoms: a comparison of scatter properties. *Med Phys* 2000; 27:894-897.
25. Jordan LK 3rd, Floyd CE Jr, Lo JY, Ravin CE. Measurement of scatter fractions in erect posteroanterior and lateral chest radiography. *Radiology* 1993; 188:215-218.
26. Thomson FJ, Paulson EK, Yoshizumi TT, Frush DP, Nelson RC. Single- versus multi-detector row CT: comparison of radiation doses and dose profiles. *Acad Radiol* 2003; 10:379-385.
27. Cristy M, Eckerman KF. Specific absorbed fractions of energy at various ages from internal photon sources. Vol 1, Method. Oak Ridge, Tenn: Oak Ridge National Laboratory, 1987.
28. International Commission on Radiological Protection. Recommendations of the International Commission on Radiological Protection ICRP Publication 60. Oxford, England: Pergamon, 1991.
29. Wagner RF, Barnes GT, Askins BS. Effect of reduced scatter on radiographic information content and patient exposure: a quantitative demonstration. *Med Phys* 1980; 7:13-18.
30. Samei E. Performance of digital radiography detectors: factors affecting sharpness and noise. In: Samei E, Flynn MJ, eds. 2003 Syllabus: categorical course in diagnostic radiology physics—advances in digital radiography. Oak Brook, Ill: Radiological Society of North America, 2003; 49-61.
31. Yaffe MJ, Rowlands JA. X-ray detectors for digital radiography. *Phys Med Biol* 1997; 42:1-39.
32. Samei E. Performance of digital radiography detectors: quantification and assessment methodologies. In: Samei E, Flynn MJ, eds. 2003 Syllabus: categorical course in diagnostic radiology physics—advances in digital radiography. Oak Brook, Ill: Radiological Society of North America, 2003; 37-47.